

## Electronic Phase Diagram of Single-Element Silicon “Strain” Superlattices

Zheng Liu,<sup>1,2</sup> Jian Wu,<sup>3</sup> Wenhui Duan,<sup>3</sup> Max G. Lagally,<sup>4</sup> and Feng Liu<sup>2,\*</sup>

<sup>1</sup>*Institute for Advanced Study, Tsinghua University, Beijing, China, 100084*

<sup>2</sup>*University of Utah, Salt Lake City, Utah 84112, USA*

<sup>3</sup>*Department of Physics, Tsinghua University, Beijing, China, 100084*

<sup>4</sup>*University of Wisconsin, Madison, Wisconsin, 53706*

(Received 30 March 2010; published 2 July 2010)

The evidence that the band gap of Si changes significantly with strain suggests that by alternating regions of strained and unstrained Si one creates a single-element electronic heterojunction superlattice (SL), with the carrier confinement defined by strain rather than by the chemical differences in conventional compositional SLs. Using first-principles calculations, we map out the electronic phase diagram of a one-dimensional pure-silicon SL. It exhibits a high level of phase tunability, e.g., tuning from type I to type II. Our theory rationalizes a recent observation of a strain SL in a Si nanowire and provides general guidance for the fabrication of single-element strain SLs.

DOI: 10.1103/PhysRevLett.105.016802

PACS numbers: 73.21.Cd, 71.70.Fk

Since the concept of superlattice (SL) was introduced by Esaki and Tsu 40 years ago [1], this artificially engineered structure has created much interest in its fundamental physics (becoming by now a textbook example for studying quantum confinement and tunneling phenomena), and inspired a wide spectrum of technological advances in quantum devices, such as quantum cascade lasers [2] and new generations of solar cells [3].

Strain is well known for band engineering and has been widely used to improve the performance of Si devices by eliminating the low-mobility bands. A number of efforts to predict the relationship between strain and the band structure of Si have been made [4]. An amount of strain that is readily achievable in Si, of the order of 1%, leads to reduction in the band gap of approximately 20% [5]. The recognition that the band gap changes with strain suggests that if one could put strained Si next to unstrained Si, one would in essence create an electronic junction, and if one could put alternate strained and unstrained Si layers in sequence, one would produce a “single-element strain SL,” with the band offsets defined by strain rather than by composition difference as in the case of conventional SLs. A recent experiment [6], in which local strain was created on the 100 nm scale using nanostressors epitaxially grown on thin Si membranes to create periodic band gap modulation in a single material, has shown an initial example of this prospect.

The single-element strain SL is fundamentally different from the conventional compositional SL. The physical mechanism to create band gap modulation is different, as illustrated in Fig. 1. In the single-element SL [Fig. 1(a)], bands are divided by a “strain interface” between the strained and unstrained states of the same material; in the compositional SL [Fig. 1(b)], bands are divided by an interface between two chemically different materials or alloy compositions. Therefore, this new SL extends the concept of “superlattice” to a single element that exists in

different structural states. It can be made in 1D nanowires or 2D nanomembranes by nanoscale self-assembly or by nanopatterning a stressor [see Fig. 2(a)] [6]. It expands the application of strain engineering to new territories, by combining locally induced strain [7] with band gap engineering [4].

The single-element strain SL has several unique advantages. One is the tunability of the band offset configuration (SL phases). In principle, all possible electronic band offset configurations can be achieved in the same SL by tuning the magnitude, sign, and period of strain. In compositional SLs the configuration of band offsets is chemically defined between any two given materials; changing composition can only change the magnitude of the band offset but not the type of SL phase. A second advantage of the single-element strain SL is that it can in principle be made in any material. The pure-Si SL is furthermore directly compatible with current Si technology. Additionally, strain tunes not only the electronic properties, but also the photonic and phonon properties. For example, if the strain period is made comparable to the wavelength of light in a single-

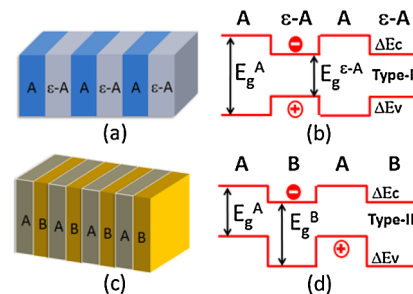


FIG. 1 (color online). Schematic illustration of a single-element strain SL and a conventional compositional SL. (a) Strain SL, in which the band offsets are provided by strain differences. (b) Compositional SL. Band alignments for either may be (c) type I, or (d) type II.

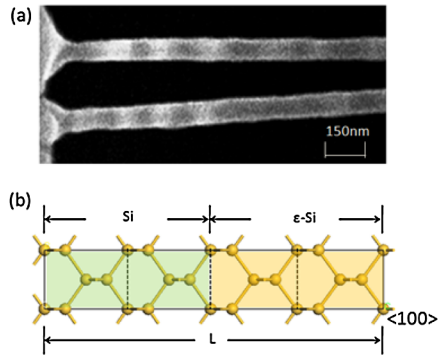


FIG. 2 (color online). (a) A top-view scanning electron microscope (SEM) image of 1D Si strain SLs fabricated by depositing Ge quantum dots (dark area) on Si (001) nanoribbons [6]. (b) The supercell structure of a Si strain SL containing two unit cells of unstrained Si and two unit cells of strained Si.

element strain SL, it automatically evolves also into a photonic crystal. As a novel form of low-dimensional nanostructure, the single-element strain SL offers a wide range of potential applications that combine the functionalities of electrons, photons, and phonons, such as in electro-optical modulators [8] and thermoelectric devices [9].

In this Letter, using first-principles calculations, we map out the electronic phase diagram for a pure-Si strain SL. We find that the SL phase can prevail only at sufficiently large strain magnitude and period, below which it will form a “strain” alloy phase. We also show that the SL phase can be tuned from type I to type II by changing the sign of the strain (compressive vs tensile). Our theory provides important guidelines for future experiments. For example, it shows that the Si nanowire structure created in Huang’s experiment [6] using SiGe nanostressors is a partial SL that confines only electrons but not holes.

In the single-element SLs, it is clear that the strain magnitude and period play the same roles as layer composition and thickness do in the conventional compositional SLs. A key parameter to characterize an electronic junction is the discontinuity of electronic bands at the interface, i.e., the band offsets. When the band gap of one layer lies entirely within that of the other layer, electrons and holes are both confined in the same layer (type I SL) [Fig. 1(b)]. In contrast, a “staggered” band lineup will confine electrons and holes in different layers (type II SL) [Fig. 1(d)]. However, when the layer thickness is very small, band offset can no longer confine the carriers. In such “short-period” SLs, the states from different layers are strongly hybridized and not distinguishable. Then, the concept of band offsets is actually meaningless and the SL behaves like an alloy [10]. Therefore, to characterize a single-element strain SL, one needs to construct its electronic phase diagram by self-consistent calculations to fully quantify the degree of carrier confinement as a function of strain magnitude ( $\epsilon$ ) and period ( $L$ ).

We have calculated band structures and charge distributions of a Si strain SL, in which uniaxial strain along the

<100> direction is periodically applied [see Fig. 2(b)]. By evaluating the degree of carrier confinement in terms of band-edge local density of states (BELDOS) as well as single-valley wave functions, we are able to construct an electronic phase diagram for the Si strain SL, shown in Fig. 3. We see that the Si strain SL exhibits a very rich phase diagram that consists of four different phases in five separate regions in the parameter space of  $\epsilon$  and  $L$ , including the phases of “strain alloy,” type I, type II, and partial SL. It demonstrates a high level of phase tunability, as all the phases can be achieved by tuning  $\epsilon$  and  $L$ . Similar calculations can be performed for any other single-element strain SLs. In the following we discuss in detail the calculations of the electronic phase diagram and its physical implications.

Our calculations are performed within the framework of density functional theory with a linear-combination-of-atomic-orbital basis as implemented in the SIESTA code [11]. The exchange-correlation functional is approximated using the Ceperley-Alder data parameterized by Perdew and Zunger [12]. Core electrons are replaced by *ab initio* norm-conserving Troullier-Martin pseudopotentials. For valence electrons, we use a double zeta polarization basis set. An equivalent plane-wave cutoff of 150 Ry is chosen to mesh the real-space grid. A fine  $k$ -space mesh in the Monkhorst-Pack scheme is chosen to ensure convergence. For Si, spin-orbital splitting of the valence bands is 0.044 eV, an order of magnitude smaller than strain-induced band splitting and thus reasonably neglected in our calculation.

The smallest unit cell of Si with one lattice vector along the <100> direction contains 4 atoms, as indicated by the dashed-line rectangles in Fig. 2(b). To model the strain effect, a supercell is constructed containing equal numbers of strained and unstrained cells. The lattice parameter for unstrained Si is calculated to be 5.417 Å, which is used as the reference of the strain-free lattice constant throughout the calculation. The lattice vector of the strained cells along the <100> direction is set to the desired strain magnitude, while the other two lattice vectors remain unchanged.

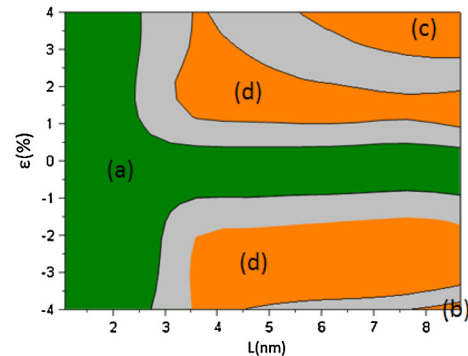


FIG. 3 (color online). Electronic phase diagram of the Si strain SL. Region (a) Strain alloy; (b) type I SL; (c) type II SL; (d) Partial SL. Light grey bands (unlabeled) are transition regions between the phases.

The atom positions in the cells simply scale with the lattice vectors. We should point out that this model neglects the strain relaxation around the interface and the Poisson effect, constrained by the supercell geometry and periodic boundary conditions. The inclusion of relaxation is beyond current computational capacity. On the other hand, finite-element analysis [6] shows that the change of axial strain magnitude at the interface is very sharp, so we expect relaxation would slightly broaden the phase boundaries, but without substantially modifying our results.

As shown by Van de Walle and Martin [13], the band offsets at the nonpolar  $A/B$  interface can be fully determined by the bulk bands of materials  $A$  and  $B$ , i.e., lining up the two sets of bands relative to a common reference level. So, the band offsets in the strain SL are fully determined by the strain-induced band shifting, i.e., the deformation potential, which has been widely studied for Si [5,14–16]. In general, the uniaxial strain, tensile or compressive, reduces the band gap of Si and leads to a type I alignment at the interface of Si and the strained Si. However, the composition of the edge states of the valence band maximum (VBM) and the conduction band minimum (CBM) changes with the sign of strain. This will embody much richer physical behavior in carrier confinement that cannot be characterized by just band offsets.

By examining the BELDOS of electrons and holes as a function of  $\epsilon$  and  $L$ , in particular, the LDOS within 30 meV from the VBM and CBM, we define a phase indicator,  $PI = \bar{D}_{Si} / \bar{D}_{\epsilon-Si}$ , the ratio of average BELDOS in the unstrained layer ( $\bar{D}_{Si}$ ) and strained layer ( $\bar{D}_{\epsilon-Si}$ ), to quantify the degree of electron or hole confinement. The limiting case of a confined phase has  $PI \sim 0$  or  $PI \sim \infty$ . For an extended carrier distribution without confinement,  $PI$  is around 1. Figures 4(a) and 4(b) show the  $PI$  results in a 2D contour as a function of  $\epsilon$  and  $L$ . The light grey area ( $PI \sim 1$ ) indicates that the electrons or holes are extended. For these values of  $\epsilon$  and  $L$ , the band structures are found to be almost identical to those of  $\epsilon/2$  uniformly strained Si, suggesting that the carriers “feel” the average strain rather than the periodic strain, which is similar to the alloy phase in a compositional SL [10]. In this sense, the strain SL in this region can be viewed as a “strain” alloy.

A clear crossover from the extended-carrier distribution phase to the confined-carrier phase can be found. The most significant confinement occurs for electrons under compressive strain. When  $\epsilon$  is higher than  $-2\%$  and  $L$  larger than 4 nm,  $\bar{D}_{\epsilon-Si}$  is an order of magnitude smaller than  $\bar{D}_{Si}$ , which suggests that the electrons can be well confined down to a 2 nm strained layer (half of  $L$ ) by compressive strain. This results from a relatively large band offset at the CBM, and also because the CBM consists of the  $\Delta_L$  valleys in the strained layer [Fig. 4(c)], which have a large effective mass in the confinement direction. In contrast, under tensile strain, the CBM comes from the  $\Delta_T$  valleys in the strained layer [Fig. 4(d)], which have a small effective mass in the confinement direction, so that no noticeable confinement is observed from the  $PI$  plot, even though

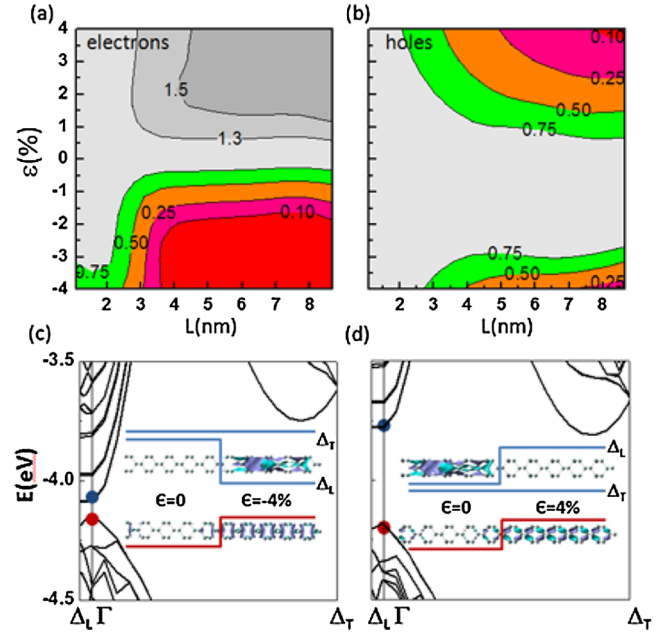


FIG. 4 (color online). Calculated isovalue contours of  $PI$  for (a) electrons and (b) holes as a function of  $\epsilon$  and  $L$ . Band diagrams of (c) type I ( $\epsilon = -4\%$ ,  $L = 5.4$  nm) and (d) type II ( $\epsilon = 4\%$ ,  $L = 5.4$  nm) Si strain SLs. The insets in (c) and (d) are schematic (not to scale) band lineups and isosurface ( $\sim 0.06 e/\text{\AA}^3$ ) plots of wave functions at the direct band edge, as indicated by the two dots at the  $\Gamma$  point.

there is still band offset at large tensile strain. The anisotropy of the effective mass of holes is not as strong as that of electrons, so that both compressive strain and tensile strain can confine holes. Typically, when the magnitude of the strain is larger than 4%, holes can be confined down to a 4 nm strained layer.

By combining the  $PI$  plot for electrons and holes, we can draw the conclusion that compressive strain with  $\epsilon < -4\%$  and  $L > 5$  nm leads to a type I SL, in which electrons and holes are both strongly confined in the strained layer. As shown in Fig. 4(c), both the CBM edge states, consisting of Kronig-Penney subbands of  $\Delta_L$  valleys, and the VBM edge states localize in the strained region. In contrast, tensile strain with  $\epsilon > 4\%$  and  $L > 5$  nm leads to a  $\Delta_L$ -valley type II SL, in which the electrons from the  $\Delta_L$  valley are confined in the unstrained layer while holes are confined in the strained layer. As shown in Fig. 4(d), the CBM edge states consist of a  $\Delta_T$  valley in the strained layer but a mixture of  $\Delta_T$  and  $\Delta_L$  in the unstrained layer. Because only the electrons in the  $\Delta_L$  valley are localized in the unstrained layer ( $\Delta_T$  electrons are extended) and all the holes are confined in the strained layer, it forms a  $\Delta_L$ -valley type II SL, in which the localized  $\Delta_L$  electrons and holes are spatially separated. We note that in both Figs. 4(c) and 4(d), there is only one single valley along the  $\Delta_T$  direction in both the strained and unstrained layers. This is a result of strong band mixing so that  $\Delta_T$  valleys always remain in the alloy phase within the calculated range.

The outcome of the  $\Delta_L$ -valley type II phase under tensile strain [Fig. 4(d)] is achieved also because the inter-valley scattering, from the  $\Delta_L$  valley in the unstrained layer to the  $\Delta_T$  valley in the strained layer, is forbidden by the selection rules. The  $\Delta_L$ -valley states in the unstrained layer have a nearly zero momentum along the  $\langle 010 \rangle$  and  $\langle 001 \rangle$  (transverse) directions, while the  $\Delta_T$ -valley states in the strained layer have large transverse momenta. Because the periodic uniaxial strain does not break the translational symmetry in the transverse directions, the hopping of carriers between the strained and unstrained layers can proceed only if their transverse momenta are conserved. Hence, it is forbidden for an electron to hop from the  $\Delta_L$  valleys in the unstrained layer to the  $\Delta_T$  valleys in the strained layer. We also note that in the unstrained layer all 6 conduction valleys are populated because the  $\Delta_L$  and  $\Delta_T$  valleys are separated by a very small energy difference (for  $\epsilon = 4\%$ ,  $L = 5.4$  nm, it is 35 meV), while in the strained layer only  $4\Delta_T$  valleys are populated because the  $\Delta_L$  valleys are of much higher energy. This makes PI to be roughly 1.5 under large tensile strain [Fig. 4(a)].

Finally, using all the calculations, including band offsets, BELDOS, and single-valley wave functions, we construct the electronic phase diagram of the Si strain SL by defining specific PI isovalues as the phase boundaries (Fig. 3). Because the crossover between different phases is gradual, the boundaries should be viewed as transition regions rather than critical points. In Fig. 3, we use  $PI < 0.2$  to identify the fully confined phase with carriers confined in the strained layer, and  $PI > 1.45$  to identify the solely  $\Delta_L$  valley confined phase with electrons confined in the unstrained layer. The width of the transition region is chosen to be  $\Delta PI = 0.2$ . After plotting the contours for both electrons and holes, the entire  $\epsilon - L$  parameter space is divided into five regions defining four distinct electronic phases. (a) Alloy. When either  $\epsilon$  or  $L$  is small, the system behaves like a strain alloy. (b) Type I SL. Compressive strain ( $|\epsilon| > 4\%$ ,  $d > 8$  nm) confines both electrons and holes in the strained layer. (c) ( $\Delta_L$  valley) Type II SL. Tensile strain ( $\epsilon > 3\%$ ,  $d > 5$  nm) confines the  $\Delta_L$  electrons in the unstrained layer, while holes are confined in the strained layer. (d) Partial SL. In these intermediate strain regions, only electrons are confined but not holes, because electrons reach the confined phase first with the increasing strain.

The phase diagram provides a useful basis for further investigations of this new type of SL. It suggests various possibilities for strain engineering to modulate the electronic properties of Si. For example, a recent experiment has shown the possibility of fabricating a strain superlattice in a SiGe nanoribbon without using the nanostressors of a second material [17]. By choosing specific combinations of strain magnitude and period, we can realize confinement for specific carriers, e.g., electrons vs holes, or  $\Delta_L$  valleys vs  $\Delta_T$  valleys. In Huang's experiment [6], the periodic strain is created on the 50–100 nm scale, but the strain

magnitude induced by the Ge quantum dots is less than 2%, so the system should stay in the partial SL phase and confinement effects can only be observed for electrons. However, type I or type II SLs are expected to be accomplished by choosing other nanostressors or using different materials as the host.

Our systematic analysis of the 1D Si strain SL has allowed us to draw some general conclusions to expand the concept of strain SL to other materials and 2D structures. In a given strain SL, the carrier confinement is a result of three factors: (1) the deformation potential, which determines the band shifting; (2) the band-edge valleys, which determine the coupling between layers; and (3) the effective mass, which determines the confinement sensitivity. All three factors are material dependent and will give rise to a material's characteristic electronic response to a periodic strain. Furthermore, in a 2D strain SL, the periodic potential is introduced in two directions; hence, the in-plane anisotropy of the effective mass of carriers is expected to result in even more interesting confinement behaviors. The unique properties of this class of low-dimensional nanoscale strain SLs, based on new fundamental physical phenomena, may enable a wide range of possible applications.

This work is supported by DOE-BES (Grants No. DE-FG02-03E46027 and No. 46028). We thank DOE-NERSC for providing the computing resources and C. Ritz for providing the image in Fig. 2(a). M. G. L. acknowledges facilities support from UW NSF/MRSEC.

---

\*fliu@eng.utah.edu

- [1] L. Esaki and R. Tsu, *IBM J. Res. Dev.* **14**, 61 (1970).
- [2] J. Faist *et al.*, *Science* **264**, 553 (1994).
- [3] C. W. Jiang and M. A. Green, *J. Appl. Phys.* **99**, 114902 (2006).
- [4] For a review, see e.g., F. Schäffler, *Semicond. Sci. Technol.* **12**, 1515 (1997).
- [5] C. Euaruksakul *et al.*, *Phys. Rev. B* **80**, 115323 (2009).
- [6] M. H. Huang *et al.*, *ACS Nano* **3**, 1305 (2009).
- [7] F. Liu *et al.*, *Nature (London)* **416**, 498 (2002).
- [8] N. K. Hon *et al.*, *Appl. Phys. Lett.* **94**, 091116 (2009).
- [9] M. S. Dresselhaus *et al.*, *Adv. Mater.* **19**, 1043 (2007).
- [10] J. Ihm, *Appl. Phys. Lett.* **50**, 1068 (1987).
- [11] P. Ordejon, E. Artacho, and J. M. Soler, *Phys. Rev. B* **53**, R10441 (1996).
- [12] D. M. Ceperley and B. J. Alder, *Phys. Rev. Lett.* **45**, 566 (1980); J. P. Perdew and A. Zunger, *Phys. Rev. B* **23**, 5048 (1981).
- [13] C. G. Van de Walle and R. M. Martin, *Phys. Rev. B* **35**, 8154 (1987).
- [14] C. G. Van de Walle, *Phys. Rev. B* **39**, 1871 (1989).
- [15] M. V. Fischetti and S. E. Laux, *J. Appl. Phys.* **80**, 2234 (1996).
- [16] D. Yu, Y. Zhang, and F. Liu, *Phys. Rev. B* **78**, 245204 (2008).
- [17] Y. Zhang *et al.*, *Appl. Phys. Lett.* **96**, 111904 (2010).